PROCEEDINGS OF SPIE

SPIEDigitalLibrary.org/conference-proceedings-of-spie

# Phasing the Webb Telescope

D. Scott Acton, Scott Knight, Maria Carrasquilla, Nick Weiser, Michaela Masciarelli, et al.

D. Scott Acton, Scott Knight, Maria Carrasquilla, Nick Weiser, Michaela Masciarelli, Sarah Jurczyk, Greg Rapp, Julio Mueckay, Erin Wolf, Jess Murphy, Larkin Carey, Eric Coppock, Chanda Walker, Joel Runnels, Garrett West, Greg Wirth, Brian Hicks, Katie Melbourne, Michael Gordon, Bob Brown, Stefano Grimaldi, Derek Sabatke, Ray Wright, Laura Coyle, Taylor Chonis, Kevin Whiteaker, Marshall Perrin, Tom Comeau, Charles-Philippe Lajoie, George Hartig, Tracy Beck, Matt Lallo, Mike Regan, Randal Telfer, Marcio Meléndez, Greg Brady, Laurent Pueyo, Nicolas Flagey, Bernard Kulp, Ed Nelan, Kiera Brooks, Pierre Chayer, Shannon Osborne, Sherie Holfeltz, Tony Sohn, Tom Zielinski, Alden Jurling, Matt Bergkoetter, Chuck Bowers, Bruce Dean, Lee Feinberg, Ritva Keski-Kuha, Jeff Kirk, Michael W. McElwain, Joe Howard, "Phasing the Webb Telescope," Proc. SPIE 12180, Space Telescopes and Instrumentation 2022: Optical, Infrared, and Millimeter Wave, 121800U (27 August 2022); doi: 10.1117/12.2633474

SPIE.

Event: SPIE Astronomical Telescopes + Instrumentation, 2022, Montréal, Québec, Canada

# Phasing the Webb Telescope

D. Scott Acton[1,*], Scott Knight[1], Maria Carrasquilla[1], Nick Weiser[1], Michaela Masciarelli[1], Sarah Jurczyk[1], Greg Rapp[1], Julio Mueckay[1], Erin Wolf[1], Jess Murphy[1], Larkin Carey[1], Eric Coppock[1], Chanda Walker[1], Joel Runnels[1], Garret West[1], Greg Wirth[1], Brian Hicks[1], Katie Melbourne[1], Michael Gordon[1], Bob Brown[1], Stefano Grimaldi[1], Derek Sabatke[1], Ray Wright[1], Laura Coyle[1], Taylor Chonis[1], Kevin Whiteaker[1], Marshall Perrin[2], Tom Comeau[2], Charles-Philippe Lajoie[2], George Hartig[2], Tracy Beck[2], Matt Lallo[2], Mike Regan[2], Randal Telfer[2], Marcio Meléndez[2], Greg Brady[2], Laurent Pueyo[2], Nicolas Flagey[2], Bernard Kulp[2], Ed Nelan[2], Kiera Brooks[2], Pierre Chayer[2], Shannon Osborne[2], Sherie Holfeltz[2], Tony Sohn, Tom Zielinski[3], Alden Jurling[3], Matt Bergkoetter[3], Chuck Bowers[3], Bruce Dean[3], Lee Feinberg[3], Ritva Keski-Kuha[3], Jeff Kirk[3], Michael McElwain[3], Joe Howard[3]

[1]Ball Aerospace and Technologies Corporation; [2]Space Telescope Science Institute; [3]NASA Goddard Space Flight Center

## Abstract

The James Webb Space Telescope (JWST) is a segmented deployable telescope, currently operating at L2. The telescope utilizes 6 degrees of freedom for adjustment of the Secondary Mirror (SM) and 7 degrees of freedom for adjustment of each of its 18 segments in the Primary Mirror (PM). After deployment, the PM segments and the SM arrived in their correct optical positions to within a ~1 mm, with accordingly large wavefront errors. A Wavefront Sensing and Controls (WFSC) process was executed to adjust each of these optical elements in order to correct the deployment errors and produce diffraction-limited images across the entire science field. This paper summarizes the application of the WFSC process.

Keywords: JWST, Webb, Wavefront Sensing and Controls, Phase Retrieval

## 1. Introduction

The James Webb Space Telescope (JWST) was launched on December 25th, 2021, after more than two decades of work performed collaboratively between NASA, The European Space Agency (ESA), and the Canadian Space Agency (CSA). After the successful deployment of the spacecraft's mechanisms [1], the Primary Mirror (PM) segments and the Secondary Mirror (SM) were also deployed—albeit millimeters rather than meters—and positioned according to our best predictions of what would constitute a perfectly aligned telescope. This is where the work of the wavefront team would begin. It would end 100 days later with diffraction-limited performance across the entire science field.

The balance of this paper describes the Wavefront Sensing and Controls (WFSC) process as it was applied to phasing the Webb telescope. We begin with a brief description of the telescope and its science instruments, along with some of the key hardware and technologies employed in WFSC. Each step in the WFSC process is described and the associated images are presented.

*scott.acton@ballaerospace.com. Phone: 303-939-5676. ball.com/aerospace

Space Telescopes and Instrumentation 2022: Optical, Infrared, and Millimeter Wave, edited by Laura E. Coyle, Shuji Matsuura, Marshall D. Perrin, Proc. of SPIE Vol. 12180, 121800U · © 2022 SPIE · 0277-786X · doi: 10.1117/12.2633474

# 2. Overview

Before discussing the application of the WFSC process, we discuss several areas that are common to the entirety.

## 2.1 The primary mirror geometry and the science instrument layout

The Webb telescope has a 6.6-meter segmented primary mirror consisting of 18 hexagons, which we number for convenience (Fig. 1, left). There are three types of segments—A's, B's and C's—with three unique prescriptions. There are 7 Science Instruments (SI's), each sampling a different part of the field of view (Fig. 1, right). The Multi-Instrument Multi-Field (MIMF) WFSC activity (section 3.10) makes use of all of the SI's to measure the field dependence of the wavefront errors. Otherwise, the WFSC process relies solely on the NIRCam modules for wavefront sensing; most frequently, the detector shown as shaded in Fig. 1. Each NIRCam module has 4 2048 X 2048 detectors, yielding 8 images. We often display these 8 NIRCam images as they present themselves on the sky (For example, as in Fig. 7). A single detector covers 1.061 arcminutes square. Unless otherwise noted, the images shown in this paper were taken using a 1% filter centered at 2.12 microns wavelength.

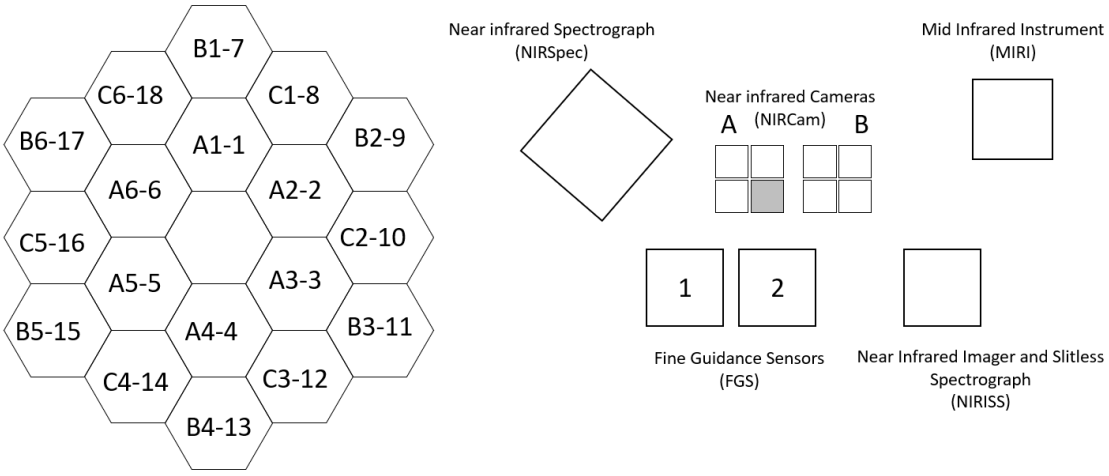


**Figure 1. The geometry of the primary mirror (left) and the layout of the science instruments (right).**

## 2.2 WFSC Guidelines

The wavefront sensing and controls algorithms and processes were developed in accordance with the following guidelines:

1. We should correct the largest errors present at a given point in the process.
2. At each step, we should try to improve the alignment of the telescope.
3. There should be generous overlap between the exit criteria of a given step and the capture range of the next step.
4. Telescope temperature must be considered (as it relates to detector and science instrument performance) as well as temperature stability (as it relates to optical alignment).
5. Minimize actuator usage.

## 2.3 Key WFSC Hardware

Rather than including a wavefront sensor as part of the observatory, the decision was made very early in the program to perform the entire telescope alignment using normal science modes of the science instruments; primarily NIRCam A and B. However, we were able to place a limited number of elements in the filter wheels of both NIRCam modules to support WFSC.

Each NIRCam module contains 3 weak lenses that can be routinely rotated into position to defocus the image, in support of Phase Retrieval (PR), which is discussed in section 2.5. Two of the lenses are placed in a filter wheel near a pupil and create +/- 8 waves of defocus when used in conjunction with a 2.12 um 1% bandpass filter. A 3$^{rd}$ lens is placed in a separate wheel and has its own 2.12 um bandpass coating. It creates +4 waves of defocus when used by itself, and -4 or +12 when used with the other two weak lenses. Counting the focused image, therefore, we have 6 unique focus positions. The weak lenses were used throughout the commissioning process and will continue to be used for wavefront maintenance operations throughout the life of the observatory.

The pupil wheels of both NIRCam modules each contain two Dispersed Hartmann Sensors (DHS) for measuring the piston errors between adjacent segments [2]. These were used in the commissioning process 3 times (Fig. 3) and are described in section 3.7.

Finally, each NIRCam module has a Pupil Imaging Lens (PIL) that can be inserted into the beam to form a coherent image of the primary mirror on one of the detectors. This image is used as a constraint in PR, as well as an overall diagnostic tool.

## 2.4 WFSC Software

A thorough description of the WFSC software is beyond the scope of this paper. A simplified view of the software is shown in Fig. 2. Image analysis is performed by the Wavefront Analysis Software (WAS). Mirror moves are also generated by the WAS. The mirror moves are converted into low-level actuator motor step commands via the Mirror Control Software (MCS). The Wavefront Executive ties these two elements together and facilitates communications with the rest of the Ground System.

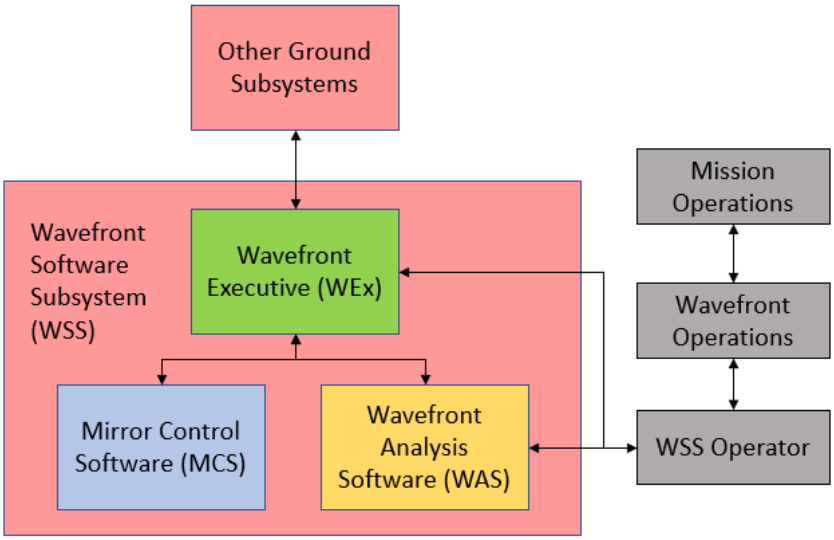


**Figure 2. The Wavefront Software Subsystem.**

## 2.5 Phase Retrieval

Phase Retrieval (PR) was used in multiple places throughout the commissioning process: Focus Sweep, Global Alignment, Fine Phasing, MIMF, and Maintenance (see Fig. 3). PR is actually a very simple concept: we find a wavefront (phase) that is consistent with the measured defocused images, and the known telescope mirror geometry (amplitude). We rely primarily on an iterative transfer algorithm [3], cross-checked by two additional independent model-based non-linear optimizer algorithms [4,5].

Fine phasing and routine maintenance operations rely on the weak lenses in NIRCam to create defocused images. Focus Sweep, Global Alignment and MIMF require moving the secondary in piston to create defocus.

Cases which have large initial segment tilt errors (such as the entrance to the second and third applications of coarse phasing) require an initial estimate to the phase in order to ensure convergence. For this we rely on a Geometrical Phase Retrieval (GPR) algorithm [6] which operates transparently within the iterative transfer algorithm.

Phase Retrieval requires at least partial coherence within the pupil. When the images are unstacked (Focus Sweep, Global Alignment), this is not an issue because we can apply PR within each individual segment. But after stacking the images, we need the piston errors to be smaller than the coherence length of the light [7] (about 100 microns) in order to apply PR. Consequently, we perform image stacking the first time based entirely on centroids. Once the piston errors are reduced, stacking can be applied using PR, which is generally a faster and more accurate approach.

In general, PR is performed using a 1% filter centered at 2.12 microns, within the A module of NIRCam. The piston errors are calculated precisely when they are within +/- ½ wave, or less than ~ 1 micron. Larger piston errors cannot be unambiguously estimated, as they present themselves modulo 2pi (or 1 wave). To mitigate this limitation, we can optionally appeal to a second wavelength (1.87 microns) which can extend the practical piston capture range to several waves.

Phase Retrieval can be performed on the other science instruments as well, although we must use the secondary mirror to create defocus. This was performed during the MIMF process (section 3.10). A modified version of the iterative transfer algorithm [8] was applied which accounts for the broadband nature of the light, and under-sampled images.

## 2.6 Actuators and Hexapods

Each PM segment and the SM has 6 actuators comprising a hexapod. This allows the segment to be moved in 3 translational degrees of freedom (radial translation, tangential translation, and piston) and 3 rotation degrees of freedom (X-tilt, Y-tilt, and clocking). Because of the radial symmetry of the primary mirror, the two translational modes are degenerate with clocking. As such, we do not use tangential translation for wavefront control. Likewise, the secondary mirror is never controlled in clocking. Each primary mirror segment also has a $7^{th}$ actuator for controlling the radius of curvature of that segment.

The actuators [9] have a dynamic range of 20 mm (~12 mm of which is used for deployment) and a step size of 7 nm, which is accomplished through coupled fine and coarse mechanisms. Whenever an actuator reaches a positive or negative limit on the fine range (~+/- 4 microns), the coarse mechanism is automatically engaged, and the fine mechanism is recentered. A consequence of engaging the coarse mechanism, however, is an uncertainty in the length of the actuator of approximately 1 micron.

Consequently, it is necessary to consider the state of the fine mechanism for each actuator at key points in the WFSC commissioning process.

### 2.7 Ground calibration

Several years before launch, the instrumental wavefront was measured at multiple field points in each science instrument [10]. During flight WFSC, this ground calibration was subtracted off from the measured wavefronts prior to acting on that wavefront. The purpose of this was two-fold: first, we wanted to avoid imprinting the wavefront at a single field point onto the entire science field, and secondly, we wanted an accurate representation of the alignment state of the telescope.

### 2.8 Simulations and Experimentation

The Webb telescope was completely aligned starting from a randomly deployed state roughly 100 times through simulations [11]. This was done to develop and vet the alignment process, but also to train operators on the WFSC technologies and software. Any anticipated difficulty was placed into the model, erring on the side of caution. As such, aligning the telescope via the simulation environment was more difficult than aligning the real telescope.

End-to-end alignment was also demonstrated multiple times on a 1/6-scale functional optical model of the telescope [12]. Much of the flight WFSC software was tested with this test bed, and we established a Technology Readiness Level (TRL) of 6 a decade before launch.

### 2.9 The WFSC process flow

A flow chart of the WFSC process is shown in Fig. 3. Each box in this chart represents a series of activities that were performed which involved moving the PM segments and the SM, taking images, and analyzing those images. Some operations (such as Global Alignment, Coarse Phasing, and Fine phasing) were applied more than once, although often with different goals. In Section 3, we describe each activity and present the associated images and analysis.

## 3. Phasing the Webb Telescope

In this section, we present the results of executing each of the activities shown in Fig. 3 on the Webb telescope during commissioning, beginning after the PM segments and the SM were deployed. We encountered 2 unexpected behaviors with the telescope that caused us to deviate slightly from our planned procedures:

1. Initially, it was difficult to control the absolute pointing of the telescope to any better than about 15 arcseconds. Eventually, the root cause of this problem was discovered and corrected. The first few activities, however, had to be accomplished in the presence of these large pointing uncertainties.
2. Use of the Fine Guidance Sensor was originally planned to start with Global Alignment 1. However, we were not able to use the FGS until Global Alignment 2, meaning that some of the early activities had to be performed without active image stabilization. Fortunately, the line-of-site jitter was small compared to our expectations, during the time scales of a single exposure. As such, the lack of image stabilization did not prove to be a limiting factor.

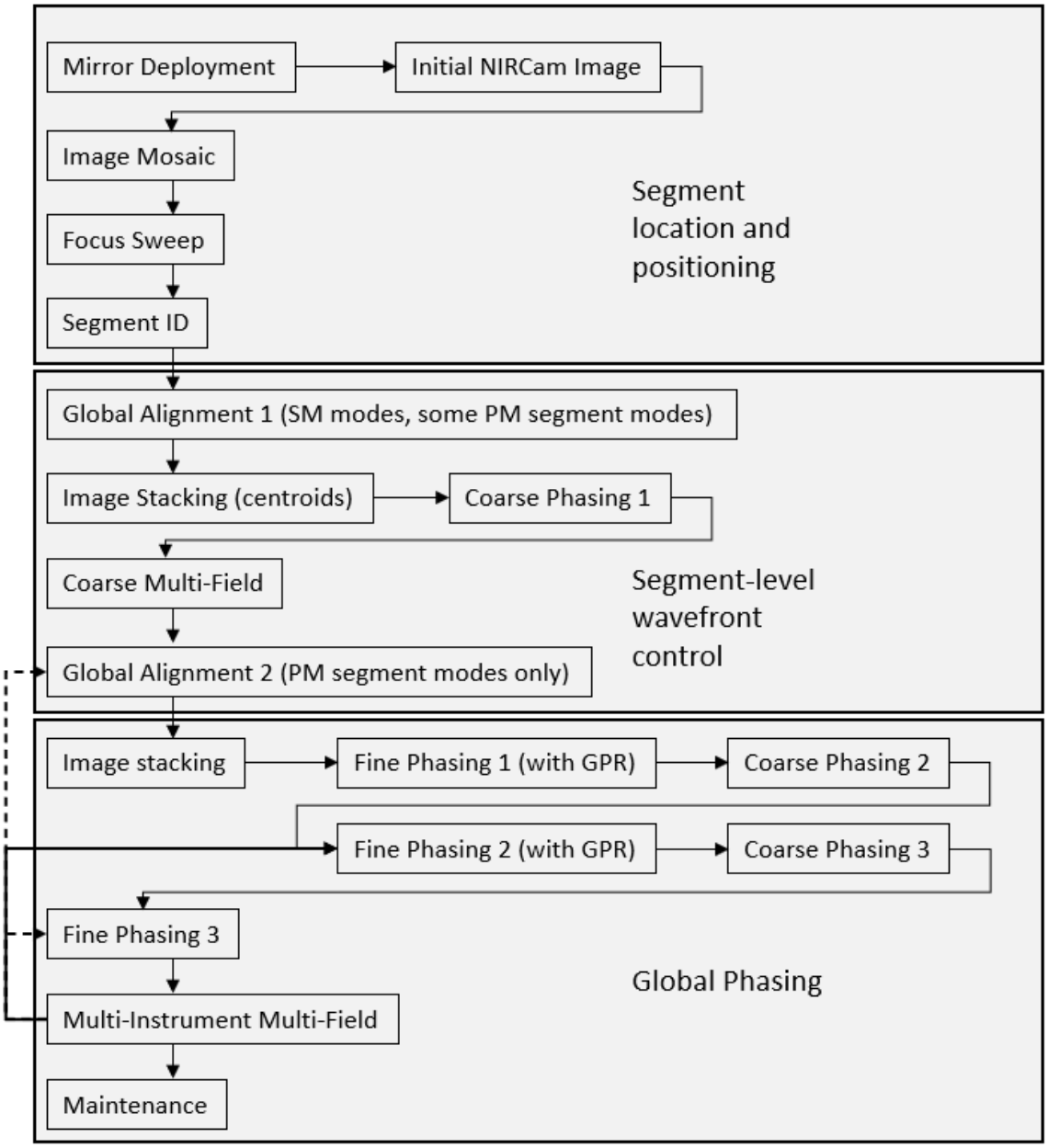


**Figure 3. The process flow diagram.**

## 3.1 Initial NIRCam Image

Although not formally part of the WFSC commissioning process, the alignment of the telescope began by pointing to a crowded field of stars (the Large Magellanic Cloud) and taking a series of images on both modules of NIRCam. An example is shown in Fig. 4. Much can be learned from this image. We can clearly see multiple “copies” of several Point Spread Functions (PSF’s) created by the same segment but from different stars. A couple of the segments exhibit pronounced astigmatism (as was expected), as well as focus errors. Primarily, however, we see that the NIRCam instruments were functioning well and that the pointing of the telescope was stable enough to take a well-exposed image.

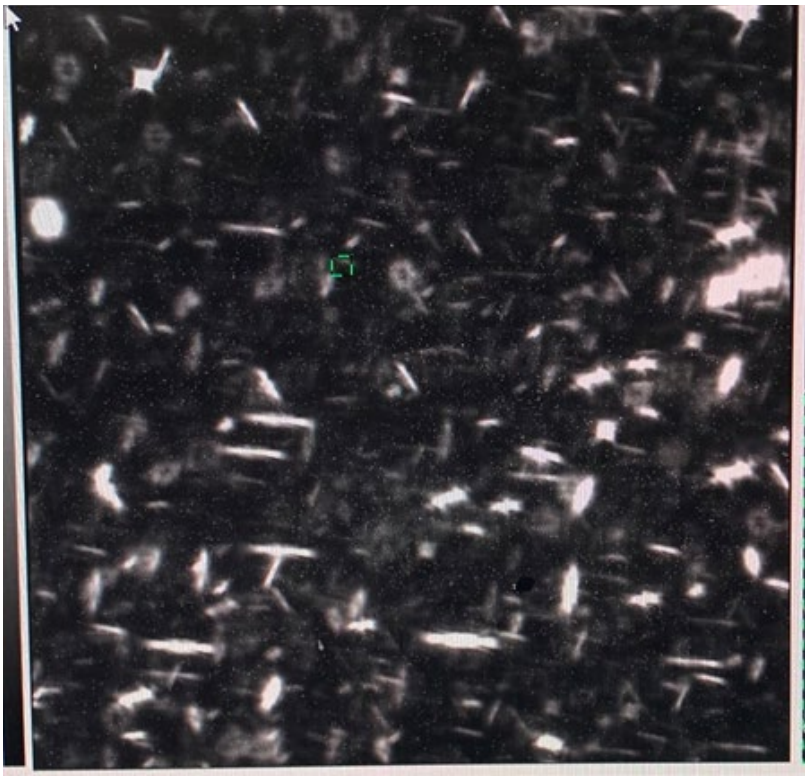

**Figure 4. Initial NIRCam image.**

## 3.2 Image Mosaic

Next, we pointed the telescope to a bright, isolated star (HD-84406). The telescope pointing was incremented along a raster pattern, taking overlapping images with both NIRCam modules simultaneously. Our plan was to stitch these images together, using the known pointing information for each position. The uncertainty in the pointing locations, however, made directly stitching the images together difficult. Fortunately, since the deployment errors of the segments were small, most NIRCam pointings contained more than one spot. We were able to stitch the images together by forcing overlap in the redundant spot(s).

In planning the image mosaic, we allowed for an initial boresight error of up to 20 arcminutes, with a comparable spread in the deployment of the individual segments. Therefore, we were prepared to take images at hundreds of positions, creating a mosaic that covered a field roughly 40 arcminutes square. In practice, it was necessary to take only a fraction of these images. The boresight error was only about 4 arcminutes, and the spread in the deployment was only 5 arcminutes. Consequently, we found all 18 spots very quickly.

The resultant image mosaic is shown in Fig. 5. The horizontal noise artifacts exist because the instrument was not yet at its optimal operating temperature. The faint arcs that are present are due to image persistence experienced while slewing, also a result of the high temperature of the instruments.

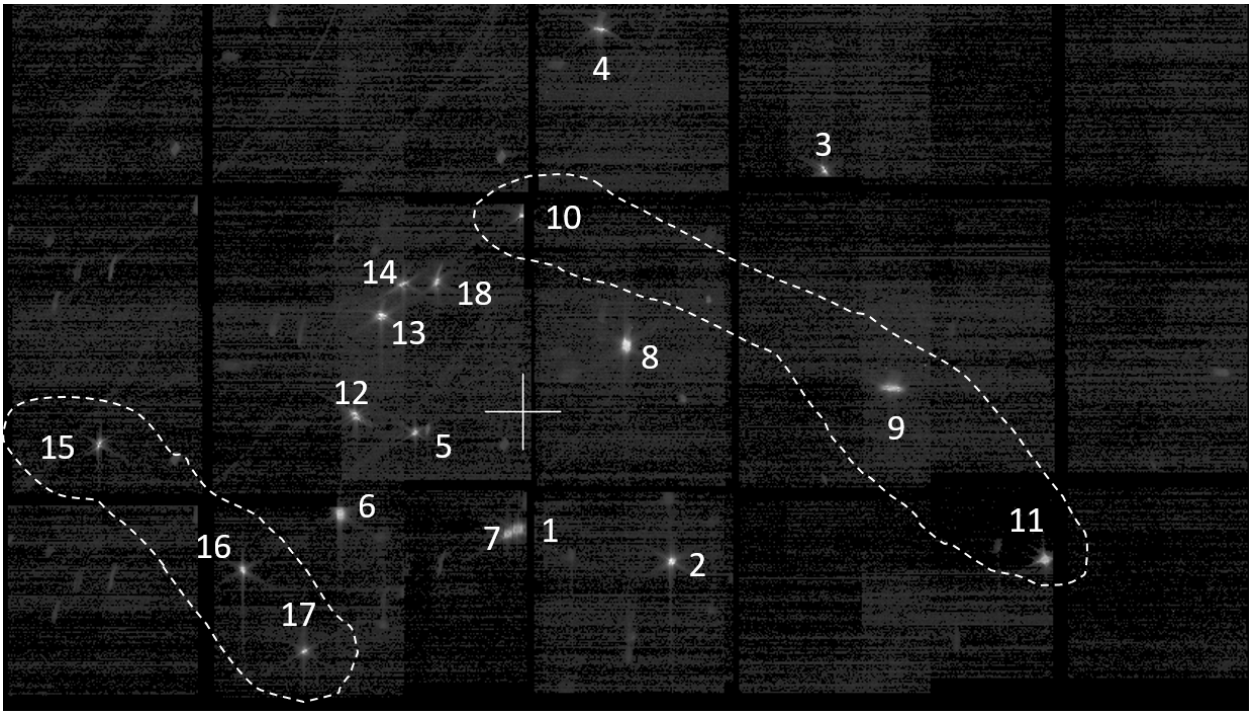


**Figure 5. The image mosaic. The segment associated with each spot is indicated by the label. The dashed lines denote the segments on the wings.**

## 3.3 Focus Sweep

Our analysis of the Image Mosaic led us to believe that there was a significant focus bias among the images that would need to be corrected before continuing with the alignment of the telescope. (The primary concern here was to guarantee that we would have spots compact enough for guiding during Global Alignment 1.) A field of view was selected that would capture the most segments in a single pointing. Images on both NIRCam modules were taken while stepping the SM through piston values of -400, -200, 0, +200, +400 microns relative to its deployed position.

The Focus Sweep software allows an operator to extract the same PSF from multiple defocus positions and estimate the phase (in particular, the focus term) from the images through the PR algorithm. By measuring the change of the centroid of the PSF at each focus position, the software also determines which segment is producing the PSFs. This is important for two reasons. First, it serves as a cross-check for the segment ID process (section 3.4). Secondly, it allows the algorithm to use the correct segment geometry in the PR (7 of the 18 segments depart from a regular hexagon). The pointing uncertainty, however, made it impossible to determine the segment from the spot motion.

Fortunately, we were able to determine the segment for each PSF another way. One of the Phase Retrievals (Fig. 6) showed a conspicuous shadow in the retrieved phase corresponding to the secondary support structure of segment 12. Since we knew precisely how segment 12's PSF should have moved when pistoning the secondary mirror, we were able to calculate the relative image motion error for all 5 focus positions, applying corrections to each group of NIRCam A and B images. Shifting these images to correct for that motion allowed us to determine the segment associated with each PSF. This is

summarized in Fig. 7, where the images from the 5 focus positions have been shifted and coadded to yield unique image motions.

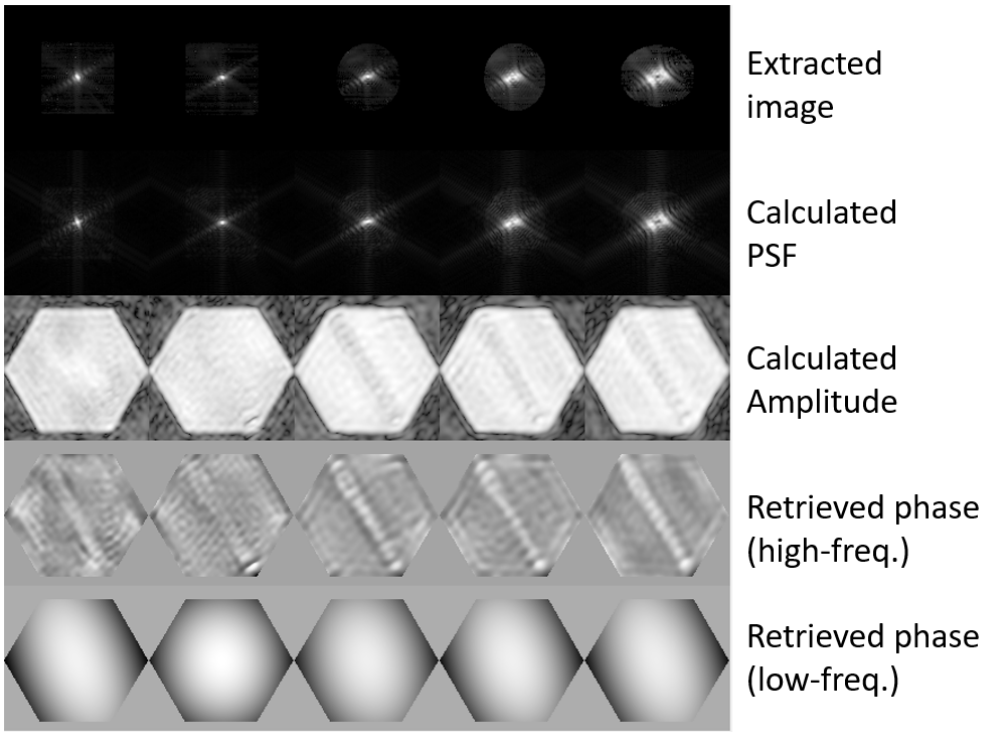


**Figure 6. An example of the PR output from the Focus Sweep.**

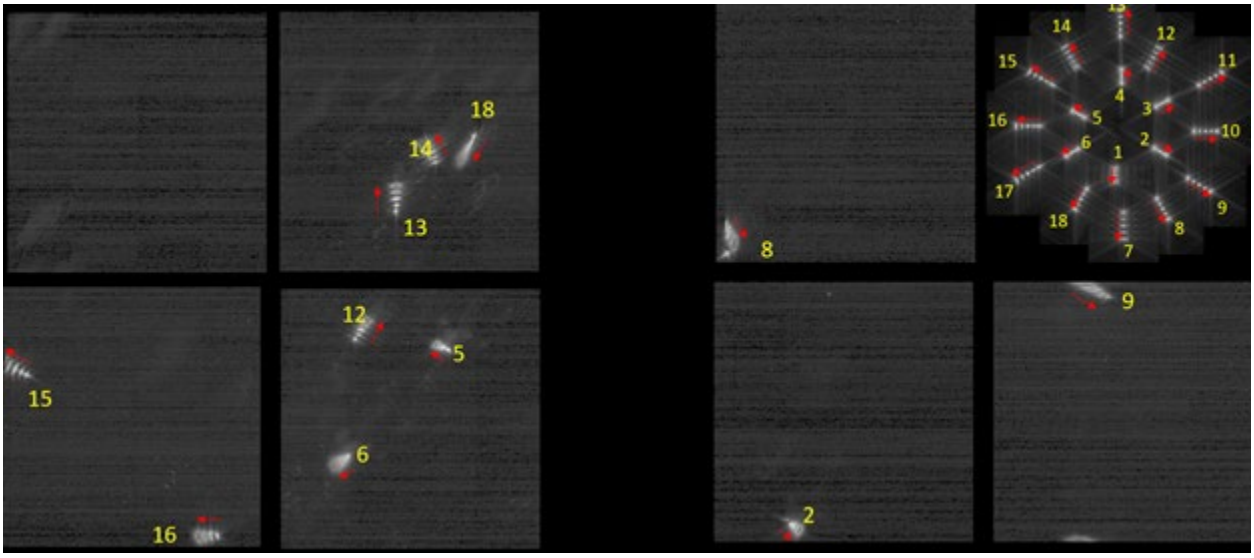


**Figure 7. Focus sweep images, correcting the pointing errors and coadding. NIRCam A is on the left; NIRCam B on the right. In the upper-right corner, we present coadded simulated images showing how each PSF should move through focus. This key was used to associate a segment with each of the PSF groups.**

Eleven image groups were analyzed to make an estimate of the optimal correction for the SM. After excluding 1 significant outlier (segment 9) we applied a correction of -427 microns to the SM piston (moving the SM away from the PM). A repeat of the focus sweep operation netted a recommended correction of only 10 microns, which was not applied. After executing the Focus Sweep, we were confident that we could continue with WFSC without any significant focus bias in the telescope.

## 3.4 Segment Identification and Image Array

The goal of the Segment ID process was to unambiguously associate each spot located in the mosaic with its corresponding segment. This would supplement the information derived in Focus Sweep, as well as identify the segments not covered in the Focus Sweep. The WFSC software takes a down-sampled version of the Image Mosaic and generates a series of telescope pointings that will capture each spot at least once, maximizing the number of captured spots in the first pointing. (In fact, the first pointing was also used for Focus Sweep.) At the first pointing, each segment was tilted so as to move the spot 200 pixels on the NIRCam detectors. Images were taken before and after each move. The WSS software analyzed the images noting which spot moved, so that we could associate that spot with the tilted segment and denoting it as “found.” The telescope was pointed to the next field, and the process was repeated for all missing segments, until all segments were found.

The only complexity associated with Segment ID is in the bookkeeping of pointing offsets, the tilting of the mirror segments, and the location of the identified segments. The purpose of this bookkeeping is so that tilts can then be generated to bring each segment into an array formed around the center of one of the NIRCam detectors. Unfortunately, the uncertainty in the telescope pointing during segment ID made absolute knowledge of the segment positions implausible.

Because of this uncertainty, we went back to the mosaic (Fig. 7) and measured the position of each segment. The positions were modified to account for the focus correction applied in Focus Sweep, and to account for the tilts applied to the segments during the Segment ID process. The geometrical center of the spots was calculated, considering only the central backplane of the primary mirror, on the assumption that the wings (that is, segments 9,10,11,15,16,17) would have higher positional uncertainty owing to their deployment mechanisms. Segment tilt commands were generated to move the spots from their current positions in the mosaic to form a small hexagonal array centered around this geometrical center. The telescope was also repointed to bring this point to the center of one of the NIRCam A detectors (the shaded detector in Fig. 1).

Each segment was tilted accordingly, taking an image after each move, so that the spot positions could be uniquely measured and moved into the correct positions in subsequent steps. The image after moving all 18 segments is shown in Fig. 8 (left). (To say that we were relieved to see all 18 spots appear on the detector would be a gross understatement!) We initially targeted a small array at the center of the detector, to minimize the chance of a spot missing the detector in the event of errors. Notice that the spots appeared spread out in the vertical direction. This is a result of the telescope cooling during the time between taking the Image Mosaic and performing this move (about 5 days).

After measuring the new spot positions, additional tilt commands were issued to bring the spots into the final image array, in preparation for Global Alignment 1 (Fig. 8, right).

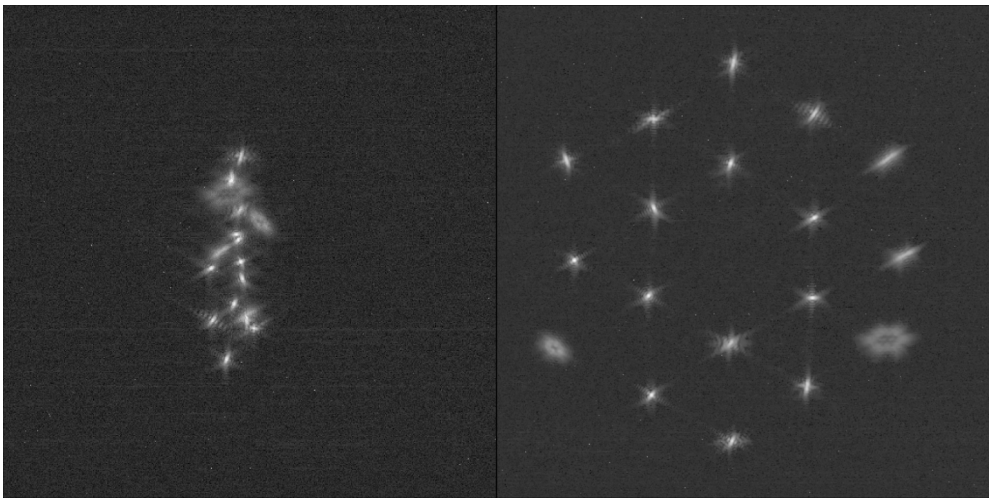

**Figure 8. Formation of the first image array after identifying the segments.**

## 3.5 Global Alignment 1 and 2

Global Alignment 1 was designed to enable us to place the SM and the PM segments in roughly the right locations—resulting in a relatively good wavefront error—early on in the commissioning process, to increase the overall accuracy of Coarse Phasing 1 and Coarse Multi-Field. With the spots in the image array, the SM is moved in piston to create defocus. As we noted in the Focus Sweep process, pistoning the SM causes the spots to move. Consequently, the PM segments are also tilted to maintain the spot positions within the image array.

The PR algorithm calculates the segment level wavefront (after removing the astigmatism terms associated with the segments being tilted away from the center.) All corrective moves are based on the power and astigmatism terms within the individual segments. Patterns in these terms can be corrected by adjusting the secondary mirror. Residual terms within an individual PM segment can be corrected by adjusting the associated segment. However, there is an unavoidable level of degeneracy:

- SM X and Y translation errors create a pattern of segment-level power and astigmatism that is indistinguishable from that created by SM X and Y tilt.
- A radius of curvature error on a segment creates primarily power; a piston error creates power as well.

We opted to correct global patterns using SM X and Y translation, since the deployment of the SM involves very large translations. Likewise, the ROC of each segment was set correctly via ground measurements, meaning that any observed power was likely the result of a PM piston error.

Global Alignment 1 was performed without fine guiding. However, the line-of-sight jitter was small enough so that the images obtained were not significantly degraded.

Images were taken with the SM piston set to -400, 0, and +400 microns. The images are shown in Fig. 9. The PR results from these images are shown at the top of Fig. 10.

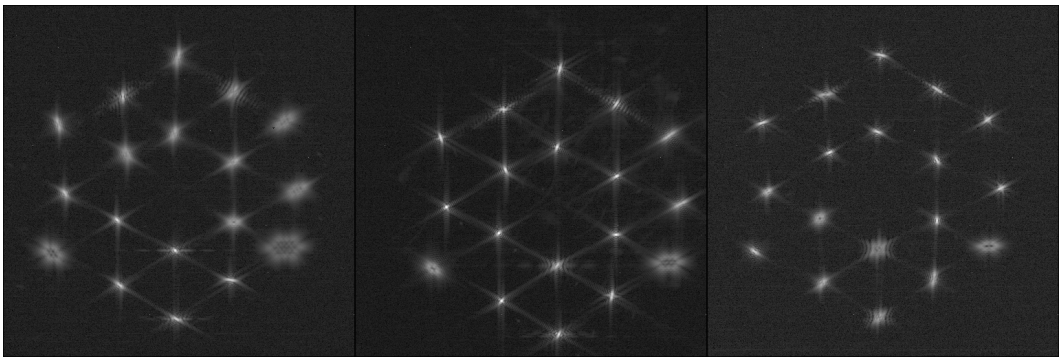

**Figure 9. Global Alignment 1 images taken -400 (left), 0 (center), and +400 (right) microns of SM piston.**

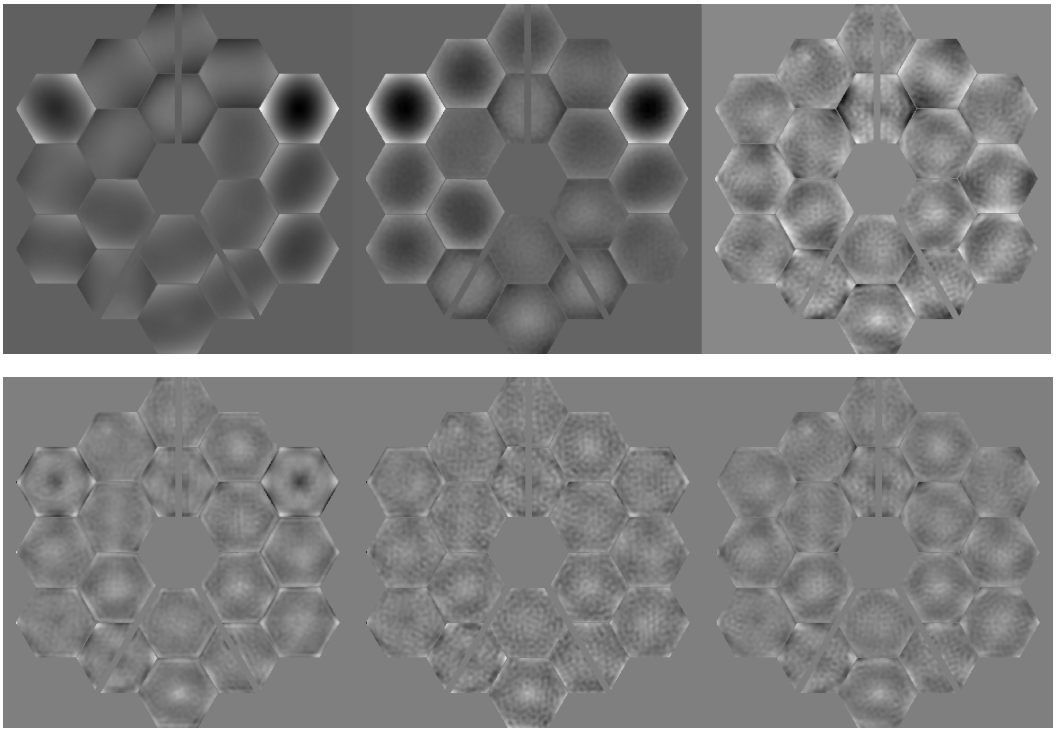

**Figure 10. Global Alignment 1 PR results. Three iterations are shown, left to right with 510, 283, 58 nm rms. Top: the raw phase results. Bottom: low-order terms through spherical aberration have been removed.**

The WAS decomposes PR results into corrective moves. The analysis indicated that an SM translation of 0.94 and 1.06 mm were required in the X and Y directions respectively. We also determined that an additional focus correction (SM piston) of +19 microns was required.

In looking at the image array (Fig. 9), and the PR results (Fig. 10) it is clear that two segments (9 and 17) are considerably more defocused than the others. We found ourselves wondering if this was due to unusually large piston errors on those segments, or if their ROC actuators were set wrong. The bottom left of Fig. 10 shows the phase after removing low-order terms up through spherical aberration. Four of the segments show a doughnut-shaped pattern with a dark spot in the middle. This is understood to be print-through resulting from a large adjustment on the Radius of Curvature ROC actuator. Two of the

segments (1 and 4) were known to have this feature. (They were polished to the wrong curvature and required an adjustment after the fact.) The other two segments showing this feature (9 and 17) was a surprise. The ROC actuators were clearly set to the wrong values. The cause of this error remains a mystery, but it was clearly the source of the large defocus term in these segments.

A correction of 1 micron was applied to the ROC mechanisms on segments 9 and 17 along with the SM translation corrections. Images were again taken with the SM piston set to +400 and -400 microns relative to the new nominal best focus.

Phase Retrieval was applied to this new pair of images, yielding the result in the upper center of Fig. 10. The global modes were examined and determined to have been corrected, to within noise levels, by the previous moves of the SM. Clocking corrections ranging from -440 to +592 microradians were generated to minimize the segment level astigmatism. Likewise, piston corrections ranging from -169 to 278 microns were generated to eliminate the power within each segment, with segments 9 and 17 requiring much larger piston corrections (~460 microns).

The large piston corrections on the two outlier segments created some concern. If we were to apply these large corrections, but instead the observed power was due to an additional ROC error, those segments would be moved outside of the capture range of Coarse Phasing (section 3.7). As a compromise, we opted to apply an additional ROC correction of 0.35 microns on each segment and correct the balance of the observed power with piston. This would minimize the chances of a capture range issue.

The above corrections were applied, and a 3$^{rd}$ set of defocused images were taken. Phase retrieval netted the phase map shown in the upper-right of Fig. 10. The residual piston and clocking corrections indicated by the phase decomposition were considered to be in the noise, and not applied. The secondary mirror was returned to the nominal focus position and the Global Alignment 1 process was concluded.

A second iteration of global alignment was applied following the Coarse Multi-Field operation (section 3.8). This was primarily a cross check of the corrections applied in Coarse Multi-Field. Small PM segment clocking and radial translations were also applied to correct astigmatism, and small ROC corrections to correct power. No changes to the SM were applied. The resultant phase map from this activity is shown in Fig. 11.

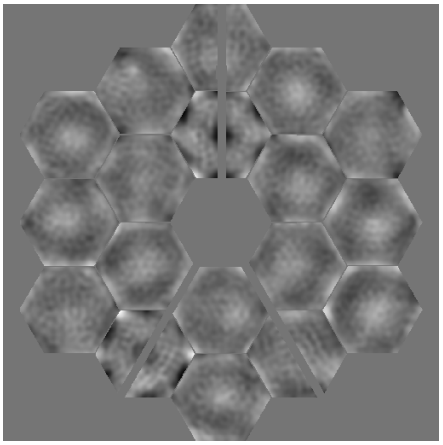

**Figure 11. The phase result achieved after Global Alignment 2. The wavefront was 44 nm rms, excluding piston and tip/tilt errors between segments.**

## 3.6 Image Stacking

The image stacking process was designed to position the images precisely on top of each other at the center of the field, while retaining the majority of the fine range in the actuators. Since large piston errors existed between the PM segments, PR would have been of little use. As a result, this image stacking process relied on centroids.

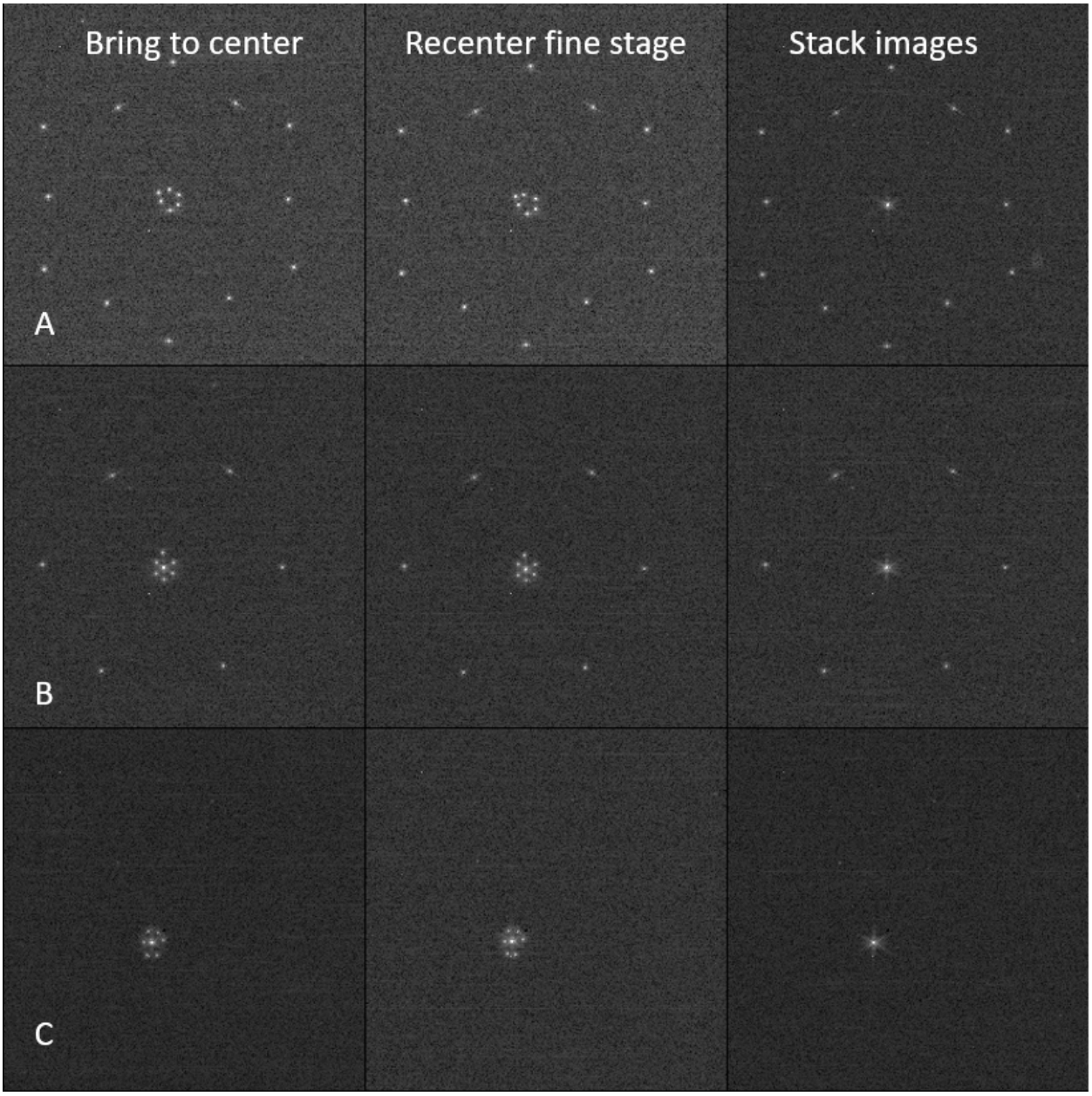


**Figure 12. Stacking the images in 3 groups; 3 steps each.**

The images were stacked in three separate groups of 6: the center (or “A”) segments, the corner (or “B”) segments, and the edge (or “C”) segments. Each group was stacked following a 3-step process:

- The segments within a group were tilted to form a small array around the stack point.
- The centroid locations were measured, and the segments were tilted to move the spots to the stack point, while intentionally engaging the coarse mechanism on each actuator and recentering the fine mechanism, and then returned to the original small array using the fine mechanisms. Engaging the coarse mechanisms created errors in the positions of the spots.
- The centroids were remeasured and spots were moved to the stack location in a very precise move, using only the fine mechanisms of the actuators.

The end state of each of these steps is shown in Fig. 12.

## 3.7 Coarse Phasing 1, 2, and 3

The purpose of Coarse Phasing is to measure--and correct--the piston errors between the individual segments. It is based on the technique of "dispersed fringe sensing" [2], which exploits the fact that a spectrum formed with a piston phase discontinuity in its pupil will exhibit a pattern resembling a barber pole (Fig. 13). The slope and pitch of the fringes in the spectra give a measure of the piston discontinuity.

Both NIRCam modules contain 2 "Dispersed Hartmann Sensors" (DHS) in their pupil wheels which individually form 10 spectra in a single image, from unique pairs of segments. Ten pairs of segments are formed in a vertical direction, and 10 are formed at a 60-degree angle (Fig. 14). The rotation of the 60-degree sensor is opposite between modules A and B, yielding a total of 30 unique pairs of segments.

After determining the relative piston difference within each pair of segments, the relative piston values between all of the segments are determined through a least-squares fit, via a pseudo-inverse operation.

The Coarse Phasing process was designed to have a capture range of about 250 microns of piston error between a pair of segments, and to have a potential sensing accuracy of about 0.25 microns (after multiple iterations). The latter accuracy is necessary in order to correct the piston errors to well below ½ wave at the fine phasing wavelength of 2.12 microns, avoiding a 2-pi ambiguity. The inherent uncertainty (~1%) associated with sensing and correcting large piston errors made it necessary to plan 3 instances of Coarse Phasing.

The first instance of Coarse Phasing was presented with very large piston errors, with 3 spectra nearing the sensing limit. The resulting piston corrections ranged from -250 to +213 microns. When applying these corrections, tip/tilt cross terms were also applied, along with ROC adjustments, in an effort to retain the stacking of the segments and cancel the power associated with the piston corrections. After concluding the first instance of coarse phasing, we moved to the Coarse Multi-Field operation (section 3.8).

As the piston errors become smaller, the sensing accuracy in Coarse Phasing degrades significantly, since there is much less signal to analyze within each spectrum. Our process mitigates this limitation by supplementing the measured spectra with a version measured after applying an additional 3 microns of piston offset on the greyed segments shown in Fig. 14. This guarantees that either the original or the offset version of each spectrum will have sufficient signal for analysis.

The second instance of coarse phasing presented us with significantly smaller piston errors. The images were analyzed, resulting in piston corrections ranging from -4 to +5 microns. Although considerably smaller than the first set of corrections, these moves also engaged the actuator coarse mechanisms, making it necessary to restack the images via the “Fine Phasing with GPR” operation as indicated in Fig. 3.

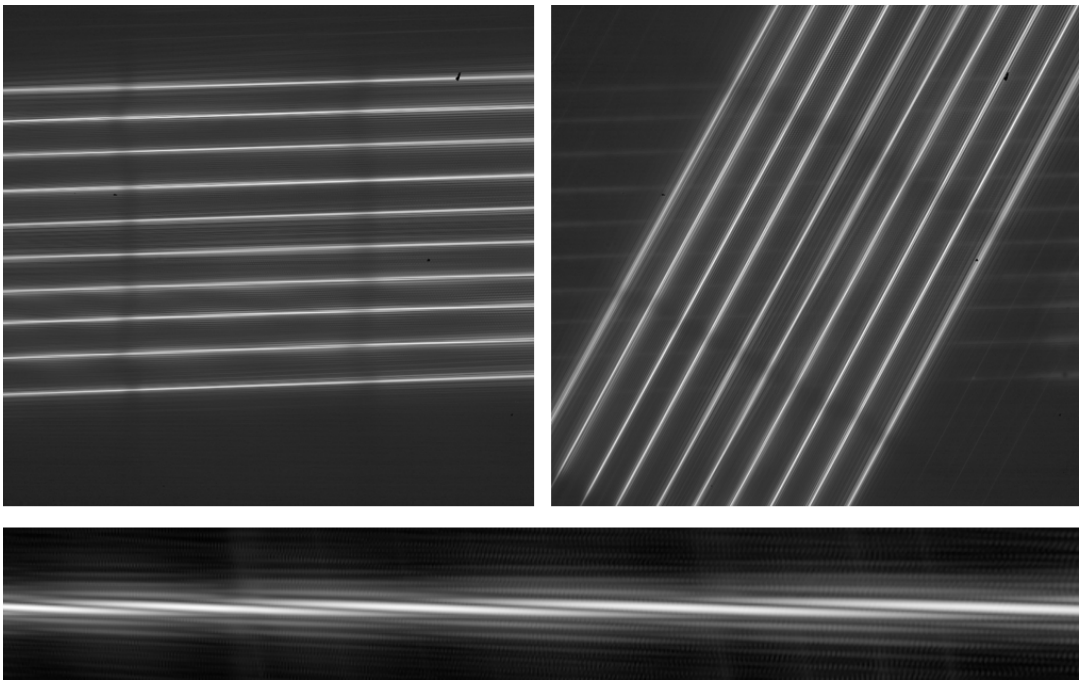

**Figure 13. DHS images from NIRCam A. Left: 0-degree spectra. Right: 60-degrees. Bottom: an extracted spectrum illustrating the barber-pole pattern.**

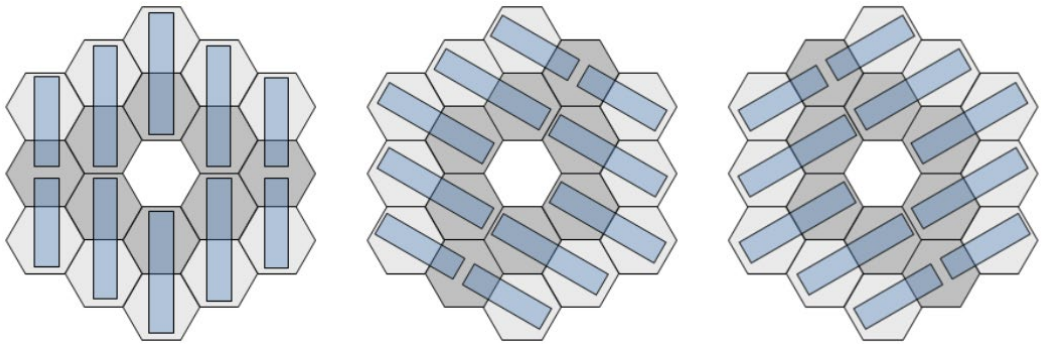

**Figure 14. Left: Vertical (0-degree) DHS elements used in both NIRCam A and B. Center: Segment pairings in NIRCam A. Right: Orientation of the DHS element in NIRCam B.**

The 3rd instance of Coarse Phasing showed very little piston error. Corrections ranged from -0.7 to +1.0 microns and did not engage the coarse mechanisms. Consequently, it was possible to transition directly into the final instance of Fine Phasing (section 3.9).

## 3.8 Coarse Multi-Field

The alignment of the telescope at a single field point is degenerate. After the corrections in Global Alignment 1, it is possible (and in fact, quite likely) that the secondary mirror is placed in the wrong position, creating global coma and astigmatism. These errors will be corrected—at a single field point—by adjusting the PM segments. Measuring at other field points, however, may reveal significant field-dependent errors. The only way to completely align the telescope, therefore, is to make wavefront measurements at a minimum of 3 non-colinear points, generating a global solution.

There is a simple linear relationship between the positioning errors of the SM and the field dependence of the wavefront errors created. Although it is beyond the scope of this paper, we will state that the field dependence can be expressed as a linear combination of field-dependent focus and astigmatism terms, derived exclusively from the SM positioning errors. By measuring this field dependence, it is possible to measure—and correct—the positioning errors of the SM. Of course, moving the SM will change the global coma and astigmatism; this must also be compensated by adjusting the PM segments [13].

In order to apply PR techniques to measuring the field dependence of the wavefront errors (section 3.10), the telescope must first be completely phased at a single field point. This takes a lot of time, and correction of any large field-dependent errors will require rephasing of the PM. AS such, we are motivated to perform the bulk of the multi-field correction early on in the commissioning process, before the PM is phased for the first time.

This technique, termed Coarse Multi-Field alignment [13] is performed after the bulk of the PM segment piston errors have been corrected, and after placing the segment PSFs into a small version of the hexagonal array. Focus and astigmatism terms are measured at 5 field points within a single NIRCam module, simply by measuring centroids along the lines of a Hartmann sensor.

Field and pupil distortion within the science instrument can affect the centroids as well. Fortunately, however, it is straightforward to show that these instrumental effects will cancel when averaging results obtained from the array, and those obtained from a version of the array that has been inverted through its center.

As previously noted, we need to adjust the PM segments in response to any SM corrections. Since we made relatively large corrections, it was convenient to include the residual wavefront errors measured at the end of Global Alignment 1 (section 3.5) and correct those errors as well.

We applied simple centroiding operations to form the image array shown in Fig. 15 (left). The spot associated with segment A2-2 was intentionally left out of the array to provide an isolated image for guiding. Images were taken at the 5 field points shown in Fig. 16 (left). Commands were then issued to form an inverted version of the array (Fig. 15, right), and measurements at the 5 field locations were repeated (Fig. 16, left).

Centroids were calculated for the 17 segments in the array, relative to the array center. Using the center group as a reference, relative spot motions at the four corner points were calculated, fitting focus and 2 astigmatism terms to each group. This was repeated for the inverted group. The focus and astigmatism coefficients were averaged between the two groups to produce a measure of the field dependence of these terms at the 4 corner field points, relative to the center, and to produce the SM moves to correct this dependence [13]. The SM corrections are shown in the center row of Table 1.

The SM corrections were applied, along with PM segment cross terms to compensate for the change in the global wavefront, and to correct the residual wavefront errors left over from Global Alignment 1 (section 3.5). Coarse mechanisms on all of the hexapod actuators were engaged, making it necessary to reform the array.

Images were taken at the 5 field points, the array was un-inverted, and the images were taken again, essentially repeating the image collection process. The centroids were processed identically, and the remaining SM corrections were again calculated. These are listed in the bottom row of table 1. These recommended corrections are quite small and are considered to be below the noise threshold of this process and, therefore, were not applied. The Coarse Multi-Field process was successful at virtually eliminating the field dependence of the wavefront errors, across NIRCam A.

The field-dependence across the other instruments was tested at the end of the WFSC commissioning using the Multi-Instrument Multi-Field process (section 3.10).

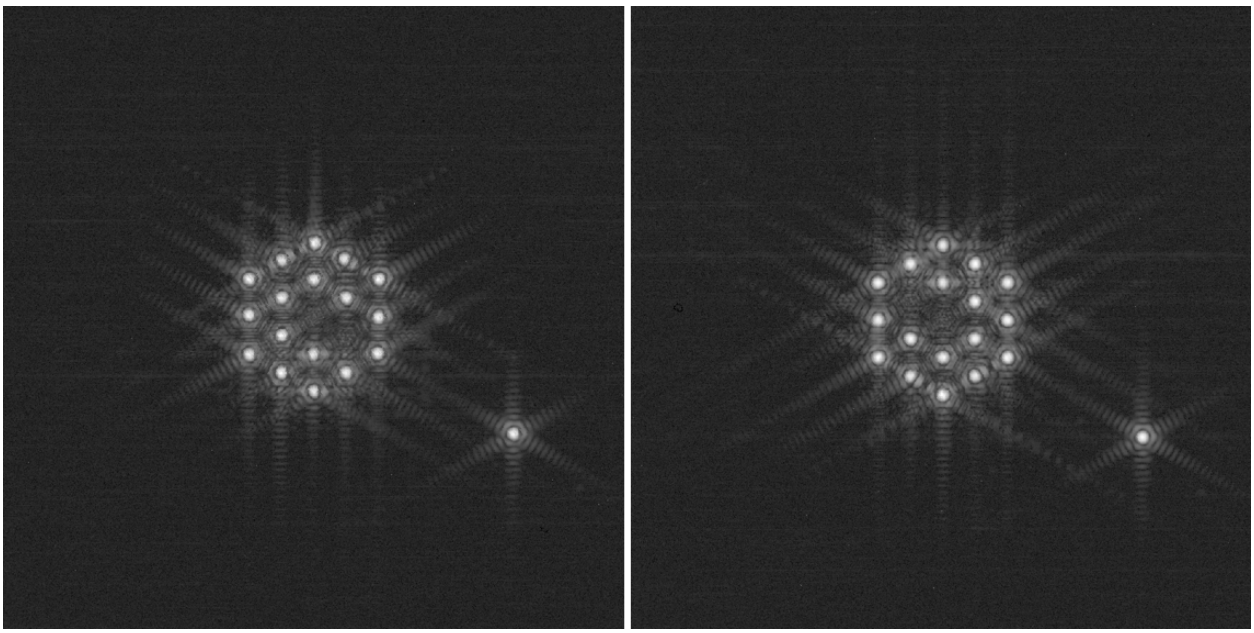

**Figure 15. Forming the medium array for Coarse Multi-Field measurements. The segment A2-2 was left in place for guiding.**

| | X translation (um) | Y translation (um) | X tilt (uRad) | Y tilt (uRad) |
|---|---|---|---|---|
| 1st iteration | -202 | 438 | -567 | -2 |
| 2nd iteration | -8 | -18 | 14 | 36 |

**Table 1. Coarse Multi-Field corrections for the secondary mirror as determined by the algorithm.**

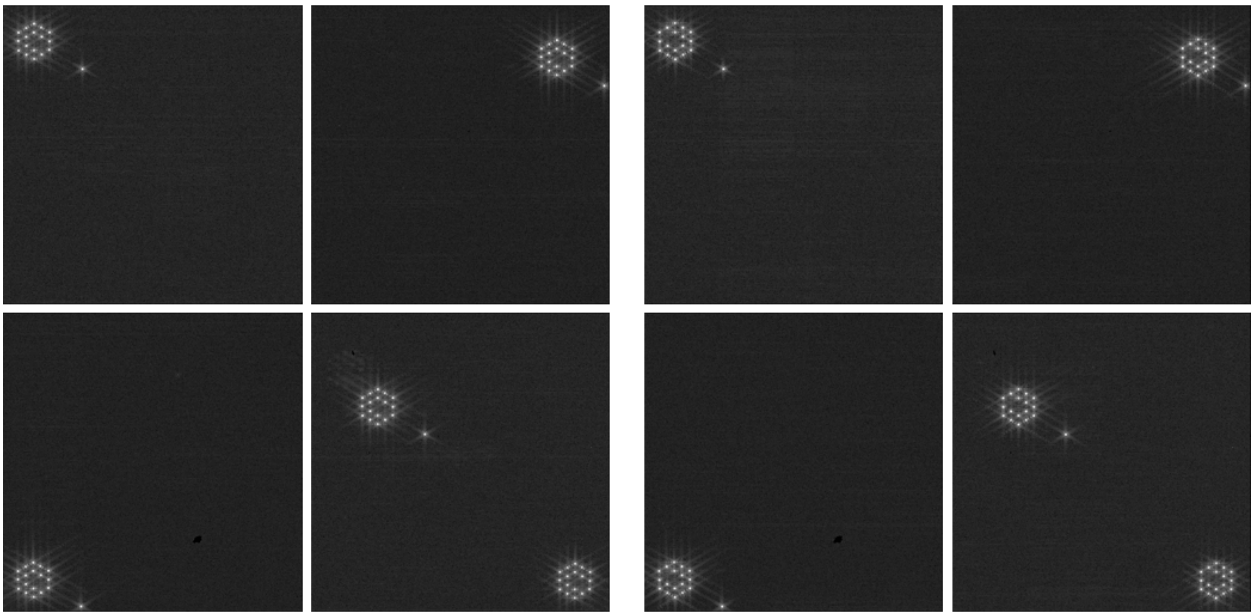

**Figure 16. Coarse Multi-Field measurements in NIRCam A with the segments in a medium array (left) and in an inverted array (right).**

## 3.9 Fine Phasing 1, 2, and 3

The Fine Phasing operations noted in Fig. 3 refer to the application of full aperture PR on defocused images taken using the Weak lenses in NIRCam. Each operation involved several iterations in order to correct the wavefront errors.

The first two applications of Fine Phasing were used to stack the segments in preparation for Coarse Phasing 2 and 3. In these two cases, only the PM segment tip and tilt errors were corrected. Guiding was initially provided on a single segment that was left in the image array, while stacking the other 17. As such, multiple iterations were applied to complete the stacking.

When using Fine Phasing for imaging stacking, it is useful to provide the PR algorithm with a good starting estimate of the segment tip/tilt errors. Towards this goal, we employed the GPR technique [6] on the 6 defocused images made available via the use of the weak lenses.

The results from the first application of Fine Phasing are shown in Fig. 17. Stacking began by commanding 17 of the segments to tilt so as to bring the spots to a common point, leaving the 18th in place for guiding. While executing these moves, the fine range mechanisms of the hexapod actuators were recentered, leaving the bulk of the range for subsequent operations. Phase Retrieval was applied on the 6 defocused images shown at the top of Fig. 17. Tip and tilt corrections were derived and applied

to stack the 17 segments. After applying these corrections, the weak lens images were retaken and are shown in the second row of Fig. 17.

The weak lens images were again analyzed with PR to confirm that the 17 images were completely stacked. Commands to refine the stacking were generated, along with commands to bring in the 18$^{th}$ segment. Guiding was switched to the stacked group, and the moves were applied. The weak lens images were taken again—they are shown in the third row of Fig. 17. The weak lens images were analyzed, resulting in one final set of corrections, primarily to completely stack the 18$^{th}$ segment. These final commands were applied, and the weak lens images were retaken. They are shown as the last row in Fig. 17.

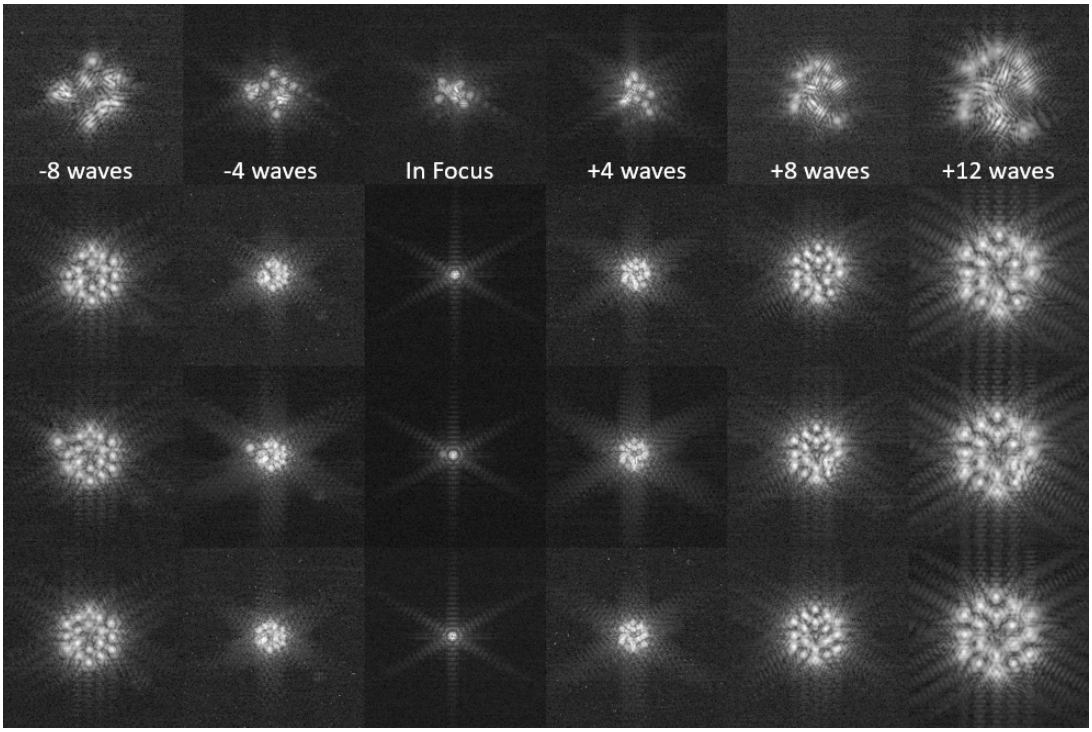


**Figure 17. Defocused images taken at the 4 steps of Fine Phasing 1.**

Following Coarse Phasing 2 corrections, the above process was repeated in order to stack the segments ahead of Coarse Phasing 3. The result of the stacking process is shown at the top of Fig. 18.

The third application of Fine Phasing was employed to correct the tip, tilt, and the piston terms, following the final set of corrections from Coarse Phasing 3, in order to completely phase the telescope. In this case, all 18 segment images were stacked at the beginning, and guiding was performed on this stacked image throughout. Small tip/tilt corrections and piston corrections were applied in two iterations (middle and bottom rows of Fig. 18.) The +/-8 wave weak lens images were also taken at a wavelength of 1.87 um to confirm that there were no 2-pi errors in the piston of the segments.

After completing the third instance of Fine Phasing, the telescope alignment was nearly complete, with the possibility of additional corrections resulting from the MIMF measurements (section 3.10).

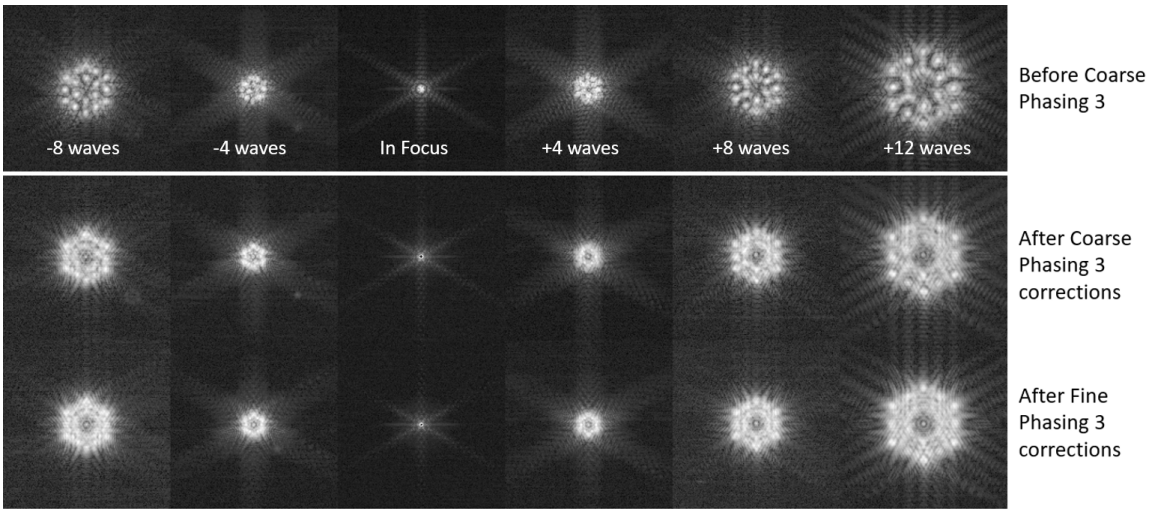


**Figure 18. The transition of the defocused images from the end of Coarse Phasing 3, to the end of Fine Phasing 3.**

## 3.10 Multi-Instrument Multi-Field (MIMF)

The Coarse Multi-Field process was designed to correct for all measurable field dependence in NIRCam A, and the bulk of the field dependence across the rest of the science field. The Multi-Instrument Multi-Field (MIMF) process was designed to sense—and correct—any residual field dependence. It was believed to be necessary owing to the relatively large extrapolation involved in extending the results from NIRCam A to the rest of the science field. In practice, however, we determined that no significant improvement in the alignment would be gained by an additional MIMF correction. The Coarse Multi-Field process was, in fact, adequate to correct the field dependence for the entire field of view.

MIMF measurements were made twice. The first measurements were made shortly after the completion of Fine Phasing 3. MIRI was not available for these measurements, as it had not yet reached its operating temperature. The second measurements were made after MIRI reached its optimal temperature, and the observatory stabilized thermally. In each case the MIMF measurements began with a series of weak lens images taken in NIRCam A. Phase retrieval was performed on these images to obtain a high-resolution phase map to use as an input to subsequent Phase Retrievals. The secondary mirror was adjusted in piston by +100 microns, to create approximately 8 microns PTV of defocus. Images were taken at 5 field points in each science instrument. The secondary mirror was then commanded to -100 microns in piston and the images were retaken at all field points. An example of defocused images from the SI's is shown in Fig 19.

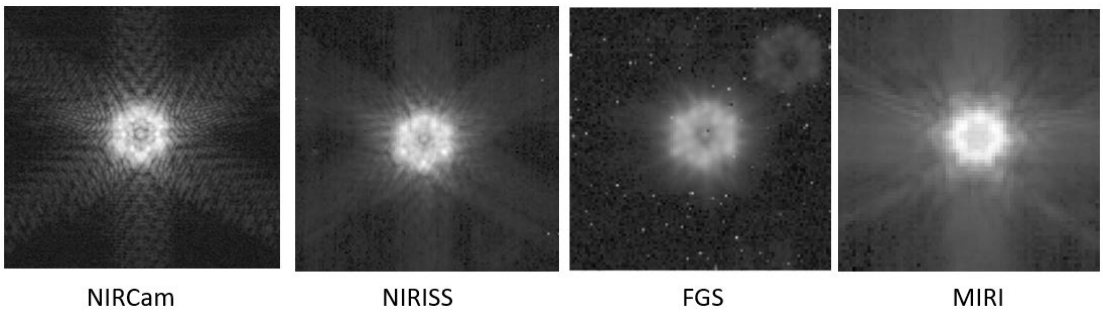


**Figure 19. Images taken with the Secondary Mirror set to -100 microns in piston.**

Phase retrieval was performed on pairs of images at each field point. Applying PR to field points outside of the NIRCam is quite challenging, for the following reasons:

- The images were broad-band (see Fig. 21).
- The images were under-sampled.
- We had to use the secondary mirror to defocus the images. (Since guiding must be performed on the defocused image, the achievable level of defocus is minimal.)

The phase errors internal to the science instrument at the selected field points [10] were subtracted to yield an estimation of the field-dependent telescope wavefronts. These are shown in Fig. 21.

The Multi-Field algorithm indicated that only small misalignments remained in the telescope, and no significant improvement in the overall science quality would result if we were to apply the recommended corrections. We did find, however, that a small focus correction (via the SM) could be applied to balance the relative focus term between the science instruments. We moved the secondary mirror by +1.8 microns, which resulted in a change in the focus term of 150 nm PTV.

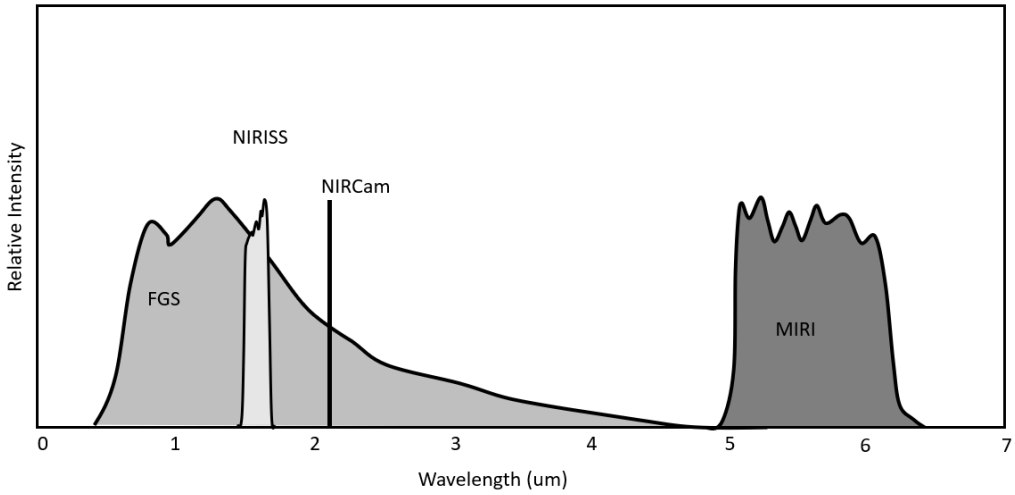


**Figure 20. Example spectra used in the Phase Retrievals. The spectra in NIRISS, FGS, and MIRI took into account the instrumental profile, the spectral type of the star, and its reddening coefficients.**

With the application of this final focus adjustment, the telescope was considered completely phased, and the WFSC processes officially came to an end.

## 3.11 Maintenance

Since completing the WFSC commissioning process, Fine Phasing images have been taken roughly every two days, resulting in corrections about 1/3 of the time. These will continue throughout the life of the observatory.

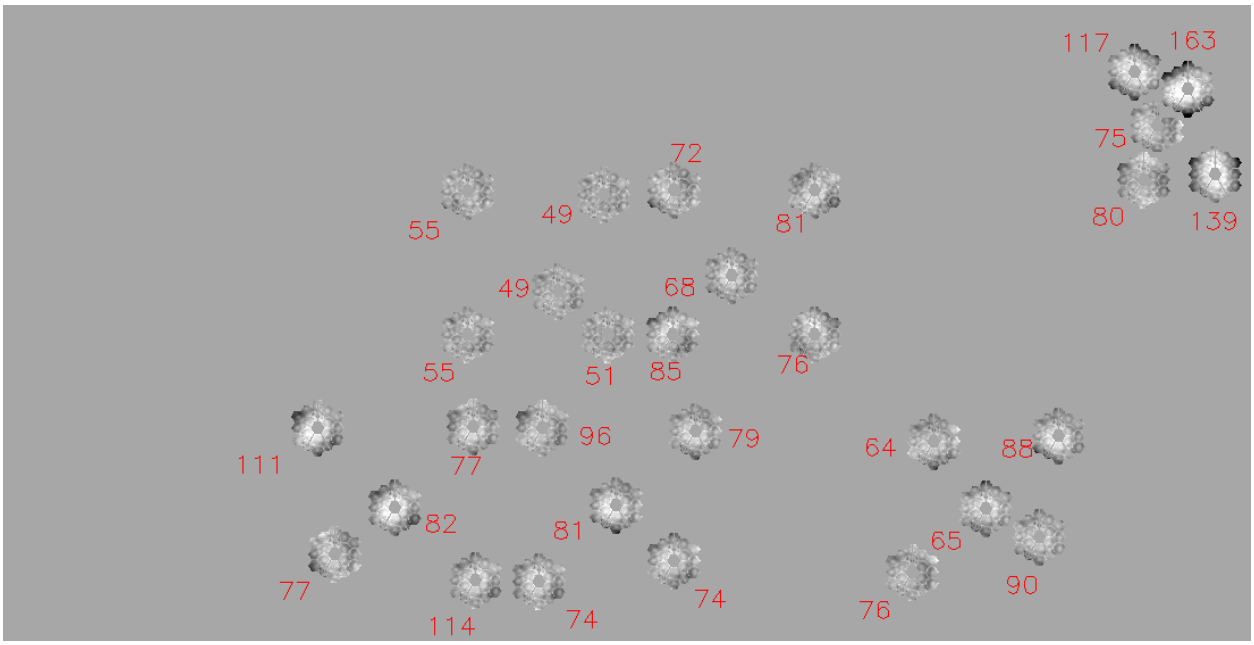


**Figure 21. The phase retrieved at each point in the science instruments (excluding NIRSpec). The rms of the phase in nm is shown.**

# 3. References


1. "Sunshield Successfully Deploys on NASA's Next Flagship Telescope." NASA Press Release, Jan 4, 2022, https://www.nasa.gov/press-release/sunshield-successfully-deploys-on-nasa-s-next-flagship-telescope.
2. F. Shi, "Experimental verification of dispersed fringe sensing as a segment phasing technique using the Keck telescope," Applied Optics, Vol. 43, No 10, p. 4474-4481, (2004).
3. B. Dean, D. Aronstein, J. S. Smith, R. Shiri, D. S. Acton, "Phase retrieval algorithm for JWST flight and testbed telescope." SPIE, Vol. 6265, (2006).
4. T. Zielinski, "Robust image-based wavefront sensing," Dissertation, University of Rochester, 2011.
5. R. Telfer, Space Telescope Science Institute, unpublished algorithm, 2022.
6. R. Carlisle and D. S. Acton, "Demonstration of extended capture range for James Webb Space Telescope phase retrieval," Applied Optics, Vol. 54, No 21, p. 6454-6460, (2015).
7. G. Ackermann, Holography: A Practical Approach (Wiley-VCH, 2007).
8. J. S. Smith, D. Aronstein, B. Dean, D. S. Acton, "Phase retrieval on broadband and under-sampled images for the JWST testbed telescope," SPIE 7436, 74360D (2009).
9. Warden, R. M., "Cryogenic Nano-actuator for JWST", Proceedings of the 38th Aerospace Mechanisms Symposium, Langley Research Center (2006).
10. D. L. Aronstein, et al., "Wavefront-error performance characterization for the James Webb Space Telescope (JWST) Integrated Science Instrument Module (ISIM) science instruments," SPIE 9904-09 (2016).
11. J. S. Knight, D. S. Acton, P. Lightsey, and A. Barto, "Integrated telescope model for the James Webb Space Telescope," Proc. SPIE 8449, 84490V (2012).

12. D. S. Acton, T. Towell, J. Schwenker, D. Shields, E. Elliott, A. Contos, K. Hansen, F. Shi, B. Dean, J. S. Smith, “End-to-end commissioning demonstration of the James Webb Space Telescope,” SPIE 6687, 668706 (2007).
13. D. Scott Acton and J. Scott Knight, “Multi-field alignment of the James Webb Space Telescope,” SPIE 8442-121, (2012).

# 4. Acknowledgements

Many people have contributed to the technology that made aligning and phasing Webb possible. 54 are listed as coauthors, and others are noted in the references. But there are undoubtably hundreds that have contributed in some form. We would like to specifically acknowledge the mentorship provided by Robert Gonsalves (Prof Emer., Tufts University), James Fienup (Prof University of Rochester), and David Redding (JPL). We also would like to acknowledge those of our team who passed away during the development of the WFSC subsytem: Russel Makidon (STScI), Richard Lyon (GSFC), and Roger Linfield (BATC).

This work was funded under NASA contract NAS5-02200.